Mathematical Modeling and Experimental Validation of a Highly Efficient Flat Plate Solar Collector with compound Transparent Insulation Materials including a Silica Layer

Rafel Febrer[1], Jesús Castro[1], Jian Zheng[1], Joaquim Rigola[1] , Asensi Oliva[1], and Deniz Kizildag[1]

[1] Heat and Mass Transfer Technological Center (CTTC) Universitat Politècnica de Catalunya-BarcelonaTech (UPC), Terrassa (Barcelona) (Spain)

Abstract

The present work consists in the development of a highly efficient solar thermal flat plate solar collector [FPC] with transparent insulation materials [TIM] at high-temperature ranges (η at $\Delta T/G$ close to 0.1 Km^2/W). The emphasis of the research is set on determining the combination of insulation materials that can boost the overall efficiency at a reasonable cost. Thus, to assess the proportions of honeycomb and granulate silica aerogel layers. A collector without a high-temperature protection system is targeted regarding the previous versions. Additionally, a fast mathematical model is being developed to predict the collector's efficiency with a high degree of confidence with low computational effort based on parallel object-oriented simulation tools. The design is tested experimentally to prove the increment in its efficiency and confirm its reliability and durability. After the simulations, a silica layer of 1cm seems to boost efficiency but does not fully protect the TIM layer of 7.5cm since temperatures are estimated to reach above 165ºC in stagnation conditions. In contrast, the thickest layer of silica simulated of 3cm decreases the temperature reached in the TIM layer by a ΔT of 30K. Thus, a overheating protection systems appears to be mandatory in any case. The experience obtained will be used to improve the next generation prototype.

Keywords: Flat plate solar collector, thermal insulation materials, silica aerogel, honeycomb

1. Introduction

FPCs have important advantages in respect to other solar collectors due to their cost-effectiveness and robustness. However, they suffer from low efficiencies working at high water inlet temperatures in cold climates compared to tubular vacuum insulated collectors. The research aims to prove that it is possible to achieve high efficiencies under the mentioned climatic conditions using a FPC.

The FPC design in the present work is based on a standard 2 m^2 surface area with a selective absorber. However, the proposed FPC has several more layers than the typical flat-plate collector. In order, from top to bottom, it has a high transmittance and low emissivity glass cover; A layer of cellulose triacetate honeycomb; Another glass layer identical to the cover layer; A layer of granular silica aerogel that has hydrophobic properties and high transmissivity in the visual spectrum and low transmissivity for infrared radiation; A selective absorber based on vertical raisers; An air gap and the back insulation (polyurethane). A graphical representation is presented in Fig. 1.

Yet the design should achieve improved efficiencies at low ambient temperatures and high inlet temperatures (η at $\Delta T/G$ close to 0.1 Km^2/W), it needs to stand high ambient temperatures and stagnation conditions. The critical point of the FPC is the honeycomb layer since this layer can be damaged if the temperatures reach a threshold. To preserve the properties of the honeycomb, the temperatures that this layer should stand should be under the range of 100ºC, the lower, the better, but never above 130-140ºC in which severe deterioration takes place as demonstrated by Giovannetti (Giovannetti et al. 2011).

In previous studies, Kessentini (Kessentini, 2014) implemented a low-cost overheating protection system that reduces the absorber temperature then the temperature of the FPC reaches a dangerous temperature. The overheating system consisted of a channel with a thermal spring-activated door. The TIGI's commercial collector followed a more expensive approach with its overheating protection system based on heat pipes (Klier

doi:10.18086/swc.2021.22.03 Available at http://proceedings.ises.org

et al. 2014). Nevertheless, the solution has drawbacks because the efficiency after the high-temperature threshold gets reduced significantly to protect the FPC.

The proposed design implements the transparent granulated silica aerogel layer to insulate and protect the honeycomb layer from the absorber temperatures while boosting the performance of the overall FPC.

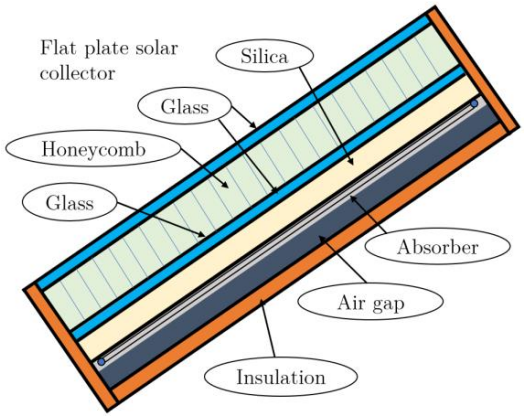

Fig. 1: Schematic representation of the FPC with transparent insulation materials (honeycomb and silica aerogel).

2. Mathematical and numerical method

One of the research objectives is to find the optimum layers' thickness or at least the best possible trade-off to maximize efficiency while keeping the costs low. Developing this process only by experimental procedures is not cost-effective; therefore, a simulation tool is required to optimize the design. Additionally, since several simulations are needed to find the optimum configuration, a fast simulation method is preferred.

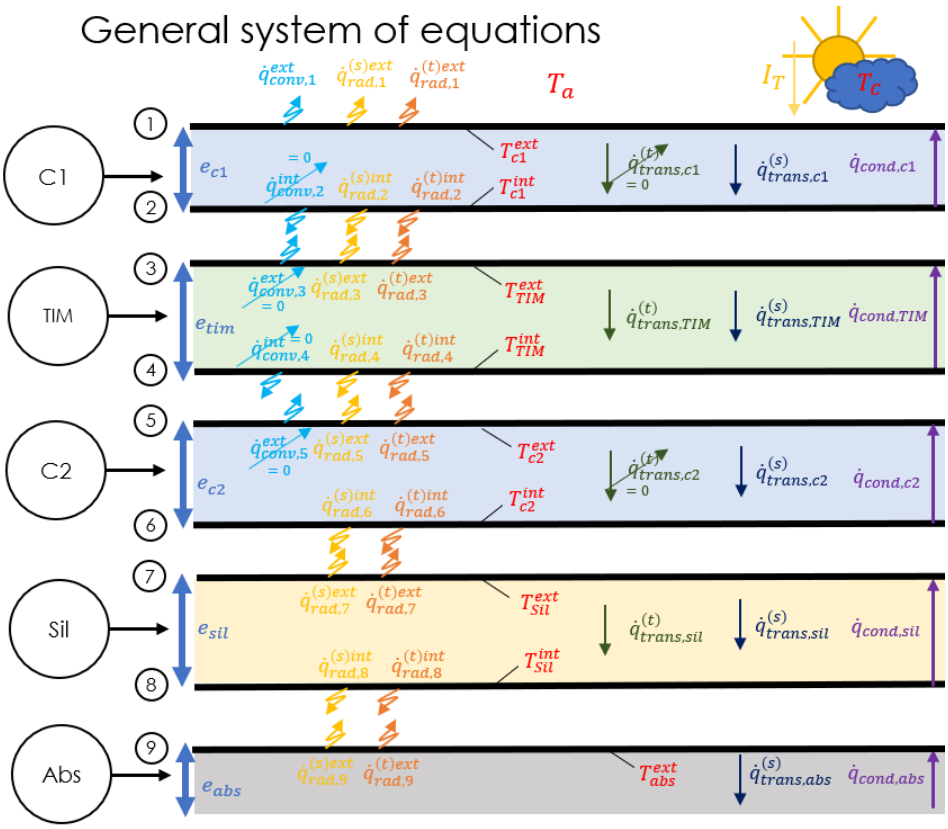

Fig. 2: Representation of heat transfer and variables for each layer

A model was implemented in a parallel object-oriented numerical platform (NEST) (Kessentini, 2014) to achieve readability and computing efficiency. The preferred mathematical approach is one-dimensional (considering the mean temperature of the layer), which assumes that each layer of material has two unique temperatures (top and bottom). The fin efficiency approach is followed to calculate the temperatures in the absorber. For the simulation of the radiation flux within the layers of the FPC, the radiosities method (Eckert Drake, 1971) is used. Since the different layers have different visible and infrared spectrum behavior, these radiations are computed separately. In that way, the properties of the honeycomb and silica layers are captured. To analyze the radiation in the model, a virtual void must be created between the layers to allow the radiosities to be computed. The heat balances in each layer are arranged to provide a system of equations. Finally, the overall heat loss coefficient is calculated, and the efficiency is estimated. Inspect Fig. 2. as a representation of the heat transfer variables considered for the calculation.

Notice that each material layer has two temperatures, the external temperature and the internal temperature, which refer to them following the logic of closer to the absorber (interior, int) or further away from it (exterior, *ext*). The infrared radiation heat transfer is identified with the suffix *t* and the visible spectrum heat transfer radiation with the suffix *s*. The overall heat transfer computed by the radiosities method is determined by the suffix *rad*, and the *trans* suffix identifies the transferred heat transfer radiation. Finally, the conduction and convection heat transfer is identified by the *cond* and *conv* suffixes.

2.1. Heat balances

To obtain the temperature values in each surface of the solar collector, it is necessary to solve a system of equations iteratively. In the current paper, three different cases (layers 1, 2, and 3) will be explained in fine detail. The system of equations will then be presented as the remaining layers extrapolate the mentioned cases.

The heat balance in layer one of the FPC can be expressed in eq.1 and Fig. 3 as the glass layer is opaque to infrared radiation, the transferred heat transfer radiation through the glass is dropped from the equation.

$$\dot{q}^{ext}_{conv,1} + \dot{q}^{(t)\,ext}_{rad,1} + \dot{q}^{(s)\,ext}_{rad,1} + \dot{q}^{(s)}_{trans,c1} = \dot{q}_{cond,c1} \qquad \text{(eq. 1)}$$

To obtain the equations to solve the system, the terms are resolved to compute the temperature of the surface 1. See eq. 2.

$$T^{ext}_{c1} = \frac{-\dot{q}^{(t)ext}_{rad,c1} - \dot{q}^{(s)ext}_{rad,c1} - \dot{q}^{(s)}_{trans,c1} + h^{ext}_{c1} T_a + \frac{k_{c1}}{e_{c1}} T^{int}_{c1}}{h^{ext}_{c1} + \frac{k_{c1}}{e_{c1}}} \qquad \text{(eq. 2)}$$

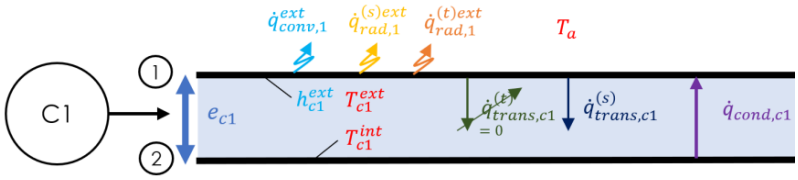

Fig. 3: Heat balance in layer 1

For layers 2 and 3, convection can be dropped from the equation since the convection inside the honeycomb layer is negligible and assumed as pure conduction (Fig. 4). Regarding the conductivity in the honeycomb, it can be computed as eq.3. The conductivity is a combination of air and honeycomb, and WF represents the honeycomb's wall fraction with respect to the air, as in Platzer (1992). In the study, the WF has been chosen as 0.011 since the honeycomb represents a small surface area of the overall plane surface of the FPC.

$$k_{TIM,eq} = WF\, k_{TIM} + (1 - WF)\, k_{air} \qquad \text{(eq. 3)}$$

The balance in layers 2 and 3 can be computed as equations 4 and 5.

$$\dot{q}^{(t)\,int}_{rad,2} + \dot{q}^{(s)\,int}_{rad,2} + \dot{q}_{cond,c1} = \dot{q}^{(s)}_{trans,c1} \qquad \text{(eq. 4)}$$

$$\dot{q}^{(t)\,ext}_{rad,3} + \dot{q}^{(s)\,ext}_{rad,3} + \dot{q}^{(t)}_{trans,TIM} + \dot{q}^{(s)}_{trans,TIM} = \dot{q}_{cond,TIM} \qquad \text{(eq. 5)}$$

To solve these equations, it is relevant to note that T^{int}_{c1} should be equal to T^{ext}_{TIM} and that $\dot{q}^{(t)\,int}_{rad,2}$ is equal to $-\dot{q}^{(t)\,ext}_{rad,3}$ and similarly, $\dot{q}^{(s)\,int}_{rad,2}$ is equal to $-\dot{q}^{(s)\,ext}_{rad,3}$. Therefore, eqs. 4 and 5 can be combined to determine the

temperature in both layers, as seen in eq. 6.

$$T_{TIM}^{ext} = T_{c1}^{int} = \frac{\dot{q}_{trans,c1}^{(s)} - \dot{q}_{trans,TIM}^{(s)} - \dot{q}_{trans,TIM}^{(t)} + \frac{k_{c1}}{e_{c1}} T_{c1}^{ext} + \frac{k_{TIM,eq}}{e_{TIM}} T_{TIM}^{int}}{\frac{k_{c1}}{e_{c1}} + \frac{k_{TIM,eq}}{e_{TIM}}} \quad \text{(eq. 6)}$$

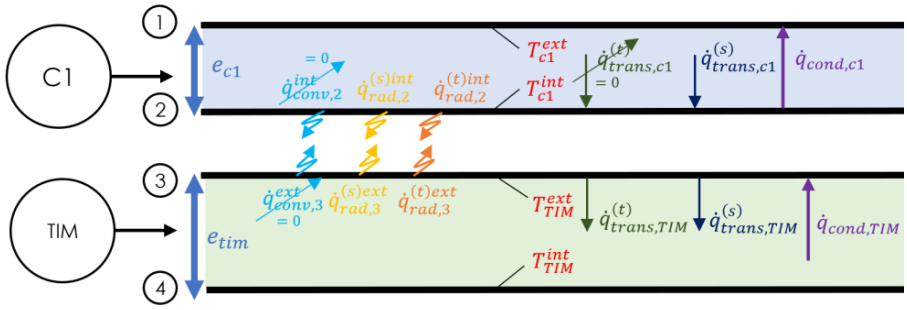

Fig. 4: Heat balance in layer 2

Following the same procedure for all the surfaces and leaving the temperatures in the function of the external temperature variables, the following system of equations can be found:

$$T_{c1}^{ext} = \frac{-\dot{q}_{rad,c1}^{(t)ext} - \dot{q}_{rad,c1}^{(s)ext} - \dot{q}_{trans,c1}^{(s)} + h_{c1}^{ext} T_a + \frac{k_{c1}}{e_{c1}} T_{TIM}^{ext}}{h_{c1}^{ext} + \frac{k_{c1}}{e_{c1}}} \quad \text{(eq. 7)}$$

$$T_{TIM}^{ext} = T_{c1}^{int} = \frac{\dot{q}_{trans,c1}^{(s)} - \dot{q}_{trans,TIM}^{(s)} - \dot{q}_{trans,TIM}^{(t)} + \frac{k_{c1}}{e_{c1}} T_{c1}^{ext} + \frac{k_{TIM,eq}}{e_{TIM}} T_{c2}^{ext}}{\frac{k_{c1}}{e_{c1}} + \frac{k_{TIM,eq}}{e_{TIM}}} \quad \text{(eq. 8)}$$

$$T_{c2}^{ext} = T_{TIM}^{int} = \frac{\dot{q}_{trans,TIM}^{(s)} + \dot{q}_{trans,TIM}^{(t)} - \dot{q}_{trans,c2}^{(s)} + \frac{k_{c2}}{e_{c2}} T_{sil}^{ext} + \frac{k_{TIM,eq}}{e_{TIM}} T_{TIM}^{ext}}{\frac{k_{c2}}{e_{c2}} + \frac{k_{TIM,eq}}{e_{TIM}}} \quad \text{(eq. 9)}$$

$$T_{sil}^{ext} = T_{c2}^{int} = \frac{\dot{q}_{trans,c2}^{(s)} - \dot{q}_{trans,sil}^{(s)} - \dot{q}_{trans,sil}^{(t)} + \frac{k_{c2}}{e_{c2}} T_{c1}^{ext} + \frac{k_{sil}}{e_{sil}} T_{abs}^{ext}}{\frac{k_{c2}}{e_{c2}} + \frac{k_{sil}}{e_{sil}}} \quad \text{(eq. 10)}$$

To complete the heat balances, it is necessary to compute the temperature in the absorber. Thus, it is followed the same approach as in section *2.4. Absorber* in Kessentini et al. (2014). The fin efficiency method is used to discretize each tube slice, as depicted in Fig. 5. Please notice that this is not a 2D discretization but a fin efficiency computation for each tube slice.

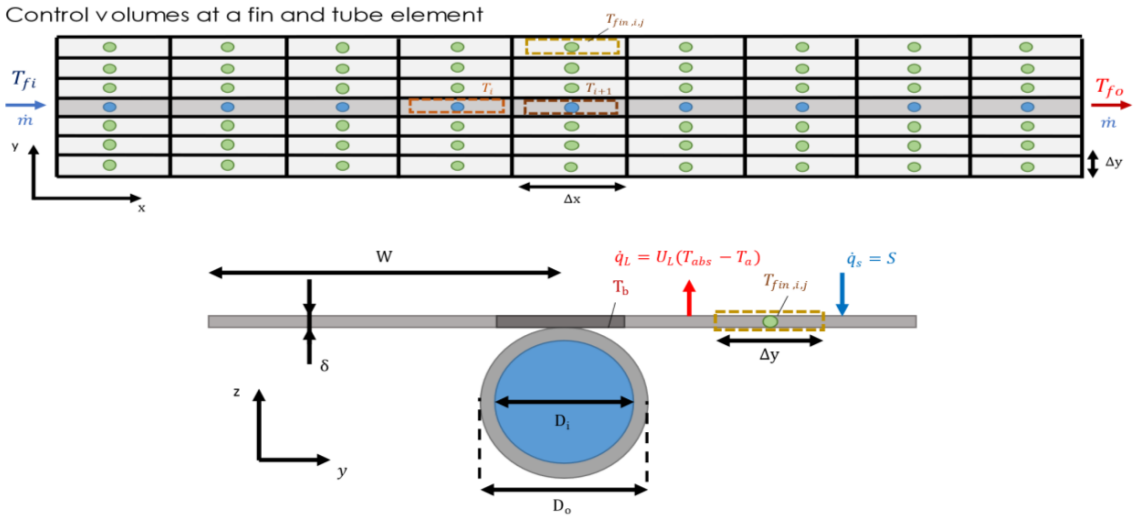

Fig. 5: Schematic representation of the control volumes at the fin and tube element of the absorber

The fin temperatures and the fluid temperatures are computed following eq. 11 and eq. 12.

$$T_{fin}^{i,j} = T_a + \frac{S}{U_L} + \left(T_{bo} - T_a - \frac{S}{U_L}\right)\frac{\cosh(my_j)}{\cosh\left(\frac{m(W-D_o)}{2}\right)} \quad \text{(eq. 11)}$$

$$T_f^i = T_a + \frac{S}{U_L} + \left(T_{fi} - T_a - \frac{S}{U_L}\right)e^{-(U_L n_t F' W x_i)/(\dot{m} c_p)} \quad \text{(eq. 12)}$$

The absorber temperature (T_{abs}^{ext}) can be computed as the mean temperature of the fins. Additionally, to calculate the overall heat transfer of the FPC, eq. 13 has been used.

$$U_L = U_{top} + U_{back} + U_{edge} = \frac{1}{R_{c1}+R_{TIM}+R_{c2}+R_{sil}} + \frac{1}{R_{ins}+R_{air\,gap}} + \frac{k_{ins}}{e_{ins}}\frac{P_c}{A_c} \quad \text{(eq. 13)}$$

In which R are the resistances produced by the several layers and P_c represent the perimeter and A_c represent the front area of the FPC. Iterating the system of equations, the temperatures in the layers can be computed and the efficiency estimated.

2.2. Radiation flux in the visible spectrum

The radiosities method is implemented to determine the radiative heat fluxes in the FPC. This method requires the computation of the view factors before the heat balances can be defined. However, in the proposed geometry, the calculation of the view factors can be solved easily with the assumption that if the layers are very close to each other, all the irradiance from one layer will impact the contiguous layer. Thus, the view factor of one layer to the other can be considered as eq. 14. The sum of the view factors should be equal to one. Therefore, the view factor of the i^{th} layer to the contiguous layer (i^{th}+1) needs to be equal to one. This simplified geometry reduces complexity in the radiosities equations.

$$F_{i,i} = 0;\ F_{i,i} + F_{i,i+1} = 1;\ F_{i,i+1} = 1 \quad \text{(eq. 14)}$$

To compute the radiosities (j) and the irradiations (ġ) is straightforward as the view factor simplifies the definition of the irradiations. For surface 1, eq.15 and eq 16 and the net heat transfer by radiation can be expressed as eq. 17. Fig. 6 represents the key variables and their position that interacted and were vital for this calculation.

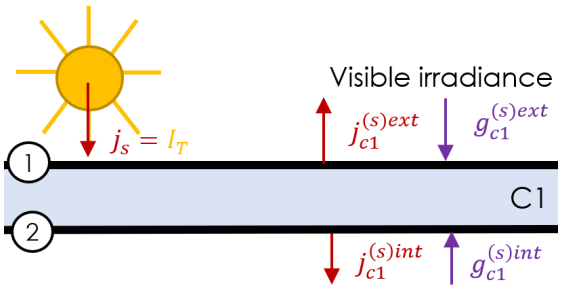

Fig. 6: Radiosities method in the glass layer for visible irradiance

$$j_{c1}^{(s)ext} = \rho_{c1}^{(s)}\dot{g}_{c1}^{(s)ext} + \tau_{c1}^{(s)}\dot{g}_{c1}^{(s)int} \quad \text{(eq. 15)}$$

$$\dot{g}_{c1}^{(s)ext} = F_{11}j_{c1}^{(s)ext} + F_{1s}j_s \quad \text{(eq. 16)}$$

$$\dot{q}_{rad,1}^{(s)ext} = j_{c1}^{(s)ext} - \dot{g}_{c1}^{(s)ext} \quad \text{(eq. 17)}$$

Finally, the transmitted heat transfer through the layer can be defined as eq.18. This heat will be used in eq. 7 and eq. 8 as an input parameter.

$$\dot{q}_{trans,c1}^{(s)} = \tau_{c1}^{(s)}\left(\dot{g}_{c1}^{(s)ext} - \dot{g}_{c1}^{(s)int}\right) \quad \text{(eq. 18)}$$

Extrapolating this procedure for all the layers, a system of equations can be prepared depending on the radiosities.

$$j_{c1}^{(s)ext} = \rho_{c1}^{(s)}\dot{g}_{c1}^{(s)ext} + \tau_{c1}^{(s)}\dot{g}_{c1}^{(s)int} = \rho_{c1}^{(s)}I_T + \tau_{c1}^{(s)}j_{TIM}^{(s)ext} \quad \text{(eq. 19)}$$

$$j_{c1}^{(s)int} = \rho_{c1}^{(s)}\dot{g}_{c1}^{(s)int} + \tau_{c1}^{(s)}\dot{g}_{c1}^{(s)ext} = \rho_{c1}^{(s)}j_{TIM}^{(s)ext} + \tau_{c1}^{(s)}I_T \quad \text{(eq. 20)}$$

$$j_{TIM}^{(s)ext} = \rho_{TIM}^{(s)} \dot{g}_{TIM}^{(s)ext} + \tau_{TIM}^{(s)} \dot{g}_{TIM}^{(s)int} = \rho_{TIM}^{(s)} j_{c1}^{(s)int} + \tau_{TIM}^{(s)} j_{c2}^{(s)ext} \quad \text{(eq. 21)}$$

$$j_{TIM}^{(s)int} = \rho_{TIM}^{(s)} \dot{g}_{TIM}^{(s)int} + \tau_{TIM}^{(s)} \dot{g}_{TIM}^{(s)ext} = \rho_{TIM}^{(s)} j_{c2}^{(s)ext} + \tau_{TIM}^{(s)} j_{c1}^{(s)int} \quad \text{(eq. 22)}$$

$$j_{c2}^{(s)ext} = \rho_{c2}^{(s)} \dot{g}_{c2}^{(s)ext} + \tau_{c2}^{(s)} \dot{g}_{c2}^{(s)int} = \rho_{c2}^{(s)} j_{TIM}^{(s)int} + \tau_{c2}^{(s)} j_{sil}^{(s)ext} \quad \text{(eq. 23)}$$

$$j_{c2}^{(s)int} = \rho_{c2}^{(s)} \dot{g}_{c2}^{(s)int} + \tau_{c2}^{(s)} \dot{g}_{c2}^{(s)ext} = \rho_{c2}^{(s)} j_{sil}^{(s)ext} + \tau_{c2}^{(s)} j_{TIM}^{(s)int} \quad \text{(eq. 24)}$$

$$j_{sil}^{(s)ext} = \rho_{sil}^{(s)} \dot{g}_{sil}^{(s)ext} + \tau_{sil}^{(s)} \dot{g}_{sil}^{(s)int} = \rho_{sil}^{(s)} j_{c2}^{(s)int} + \tau_{sil}^{(s)} j_{abs}^{(s)ext} \quad \text{(eq. 25)}$$

$$j_{sil}^{(s)int} = \rho_{sil}^{(s)} \dot{g}_{sil}^{(s)int} + \tau_{sil}^{(s)} \dot{g}_{sil}^{(s)ext} = \rho_{sil}^{(s)} j_{abs}^{(s)ext} + \tau_{sil}^{(s)} j_{c2}^{(s)int} \quad \text{(eq. 26)}$$

$$j_{abs}^{(s)ext} = \rho_{abs}^{(s)} \dot{g}_{abs}^{(s)ext} = \rho_{abs}^{(s)} j_{sil}^{(s)int} \quad \text{(eq. 27)}$$

Finally, the heat transferred through the layers can be computed as:

$$\dot{q}_{trans,c1}^{(s)} = \tau_{c1}^{(s)} \left(\dot{g}_{c1}^{(s)ext} - \dot{g}_{c1}^{(s)int} \right) = \tau_{c1}^{(s)} \left(I_T - j_{TIM}^{(s)ext} \right) \quad \text{(eq. 28)}$$

$$\dot{q}_{trans,TIM}^{(s)} = \tau_{TIM}^{(s)} \left(\dot{g}_{c1}^{(s)ext} - \dot{g}_{c1}^{(s)int} \right) = \tau_{TIM}^{(s)} \left(j_{c1}^{(s)int} - j_{c2}^{(s)ext} \right) \quad \text{(eq. 29)}$$

$$\dot{q}_{trans,c2}^{(s)} = \tau_{c2}^{(s)} \left(\dot{g}_{c1}^{(s)ext} - \dot{g}_{c1}^{(s)int} \right) = \tau_{c2}^{(s)} \left(j_{TIM}^{(s)int} - j_{sil}^{(s)ext} \right) \quad \text{(eq. 30)}$$

$$\dot{q}_{trans,sil}^{(s)} = \tau_{sil}^{(s)} \left(\dot{g}_{c1}^{(s)ext} - \dot{g}_{c1}^{(s)int} \right) = \tau_{sil}^{(s)} \left(j_{c2}^{(s)int} - j_{abs}^{(s)ext} \right) = S \quad \text{(eq. 31)}$$

This system of equations will be used as input to solve the equations defined in 2.1.

2.3. Radiation flux in the infrared spectrum

As done in the previous section, the radiosities method is applied to compute the infrared radiation. The view factors can be calculated similarly as in section 2.2. However, implementing the radiosities (j) and the irradiations (g) is not as simple as explained in section 2.2. The surfaces can emit in the infrared spectrum and need to be considered for the calculation. For surface 1, eq.32 and eq 33 and the net heat transfer by radiation can be expressed as eq. 34. In contrast with 2.2., the sky temperature (T_C) needs to be considered instead of the heat flux coming from the sun. It is assumed that the glass is opaque to the infrared irradiance, and consequently, the transmissivity is equal to zero. This won't be the case for the honeycomb and the silica layers. Fig. 7 represents the key variables and their position that interacted and were relevant for this calculation.

$$j_{c1}^{(t)ext} = \varepsilon_{c1}^{(t)} \sigma T_{c1}^{ext\,4} + \rho_{c1}^{(t)} \dot{g}_{c1}^{(s)ext} + \tau_{c1}^{(t)} \dot{g}_{c1}^{(t)int} = \varepsilon_{c1}^{(t)} \sigma T_{c1}^{ext\,4} + \rho_{c1}^{(t)} g_{c1}^{(s)ext} \quad \text{(eq. 32)}$$

$$g_{c1}^{(t)ext} = F_{11} j_{c1}^{(t)ext} + F_{1C} j_C = j_C = \sigma T_C^{\,4} \quad \text{(eq. 33)}$$

$$\dot{q}_{rad,1}^{(t)ext} = j_{c1}^{(t)ext} - g_{c1}^{(t)ext} \quad \text{(eq. 34)}$$

The transmitted heat transfer is zero in this layer, but it will be expressed as if it was not, as an example. It is defined in eq. 35.

$$\dot{q}_{trans,c1}^{(t)} = \tau_{c1}^{(t)} \left(\dot{g}_{c1}^{(t)ext} - \dot{g}_{c1}^{(t)int} \right) = 0 \quad \text{(eq. 35)}$$

Extrapolating this procedure for all the layers, a system of equations can be prepared depending on the radiosities.

$$j_{c1}^{(t)ext} = \varepsilon_{c1}^{(t)} \sigma T_{c1}^{ext\,4} + \rho_{c1}^{(t)} \sigma T_C^{\,4} \quad \text{(eq. 36)}$$

$$j_{c1}^{(t)int} = \varepsilon_{c1}^{(t)} \sigma T_{c1}^{int\,4} + \rho_{c1}^{(t)} j_{TIM}^{(t)ext} \quad \text{(eq. 37)}$$

$$j_{TIM}^{(t)ext} = \varepsilon_{TIM}^{(t)} \sigma T_{TIM}^{ext\,4} + \rho_{TIM}^{(t)} j_{c1}^{(t)int} + \tau_{TIM}^{(s)} j_{c2}^{(s)ext} \quad \text{(eq. 38)}$$

$$j_{TIM}^{(t)int} = \varepsilon_{TIM}^{(t)} \sigma T_{TIM}^{int\,4} + \rho_{TIM}^{(s)} j_{c2}^{(s)ext} + \tau_{TIM}^{(s)} j_{c1}^{(s)int} \quad \text{(eq. 39)}$$

$$j_{c2}^{(t)ext} = \varepsilon_{c2}^{(t)} \sigma T_{c2}^{ext\,4} + \rho_{c2}^{(s)} j_{TIM}^{(s)int} \quad \text{(eq. 40)}$$

$$j_{c2}^{(t)int} = \varepsilon_{c2}^{(t)} \sigma T_{c2}^{int\,4} + \rho_{c2}^{(s)} j_{sil}^{(s)ext} \quad \text{(eq. 41)}$$

$$j_{sil}^{(t)ext} = \varepsilon_{sil}^{(t)}\sigma T_{sil}^{ext\,4} + \rho_{sil}^{(s)} j_{c2}^{(s)int} + \tau_{sil}^{(s)} j_{abs}^{(s)ext} \quad \text{(eq. 42)}$$

$$j_{sil}^{(t)int} = \varepsilon_{sil}^{(t)}\sigma T_{sil}^{int\,4} + \rho_{sil}^{(s)} j_{abs}^{(s)ext} + \tau_{sil}^{(s)} j_{c2}^{(s)int} \quad \text{(eq. 43)}$$

$$j_{abs}^{(t)ext} = \varepsilon_{abs}^{(t)}\sigma T_{abs}^{ext\,4} + \rho_{abs}^{(s)} j_{sil}^{(s)int} \quad \text{(eq. 44)}$$

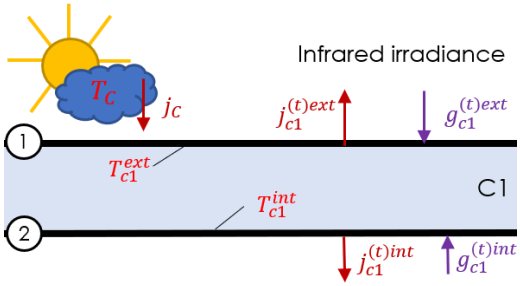

Fig. 7: Radiosities method in the glass layer for infrared irradiance

Finally, the heat transferred through the layers can be computed as:

$$\dot{q}_{trans,c1}^{(t)} = \tau_{c1}^{(t)}\left(\dot{g}_{c1}^{(t)ext} - \dot{g}_{c1}^{(t)int}\right) = 0 \quad \text{(eq. 45)}$$

$$\dot{q}_{trans,TIM}^{(t)} = \tau_{TIM}^{(t)}\left(\dot{g}_{c1}^{(t)ext} - \dot{g}_{c1}^{(t)int}\right) = \tau_{TIM}^{(t)}\left(j_{c1}^{(t)int} - j_{c2}^{(t)ext}\right) \quad \text{(eq. 46)}$$

$$\dot{q}_{trans,c2}^{(t)} = \tau_{c2}^{(s)}\left(\dot{g}_{c1}^{(t)ext} - \dot{g}_{c1}^{(t)int}\right) = 0 \quad \text{(eq. 47)}$$

$$\dot{q}_{trans,sil}^{(t)} = \tau_{sil}^{(t)}\left(\dot{g}_{c1}^{(t)ext} - \dot{g}_{c1}^{(t)int}\right) = \tau_{sil}^{(t)}\left(j_{c2}^{(t)int} - j_{abs}^{(t)ext}\right) \quad \text{(eq. 48)}$$

This system of equations will be iterated in parallel with the equations defined in 2.1 since it depends on the temperatures. The output of equations 45 to 48 will also serve as an input to the system of equations 2.1.

2.4. Remarks of the mathematical model

The numerical method proposed can be computed in a parallel object-oriented way because it needs several iterations to converge. Since some equations are quadratic, a relaxation factor of 0.9 is used to improve convergence.

Additionally, the optical and thermal properties considered in the present document will not be discussed in great detail. In the concrete case of the silica properties, they are not straightforward to estimate and require their proper discussion. As a generical introduction to the silica layer, it is necessary to emphasize that its thermal conductivity is affected by temperature (Fig. 8), and its transmissivity in the infrared spectrum needs to be estimated. Moreover, the conductivity provided by manufacturers should be reformulated to incorporate the radiosities method with the silica layer. The difference between the apparent conductivity in Fig. 8 and the thermal conductivity as used in the equation previously described consists of the apparent conductivity considering the optical properties in the infrared spectrum of the silica layer in an implicit way. This component should be extracted from the apparent conductivity and computed separately to compute radiosities.

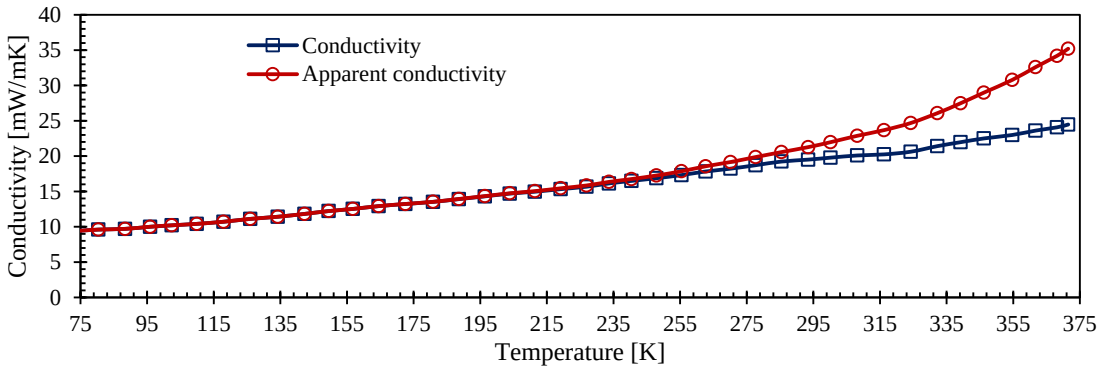

Fig. 8: Comparison of the apparent conductivity of the silica vs. the thermal conductivity

Regarding the honeycomb layer, the transmissivity in the visible spectrum requires computing both the direct and the diffuse solar irradiance independently (the transmissivity of the honeycomb is lower for the diffuse irradiance), which makes the computation depends on the weather conditions. The direct transmissivity of the honeycomb is estimated in a conservative way to be 0,9 and the difusse irradiance transmissivity close to 0,87. The difuse ratio has been estimated to be of the 36% as it has been the average during the experimental period.

Nevertheless, glass and absorber optical properties can be defined as per the manufacturer's data without increased complexity.

3. Experimental data vs. numerical method

The experimental collector was manufactured according to the simulation's mathematical results and to prove the mathematical model.

3.1. Experimental setup

An experimental test bench is used to obtain the steady-state efficiency of the collector (see Fig. 9.). All the experimental data was registered and averaged by 15-minute periods on maximum irradiance conditions (incidence angle of 0º). The FPC was tested under different inlet temperature conditions to obtain the efficiency curve. The steady efficiency curve of the FPC has been obtained according to ISO 9806-1:1994 in the CTTC SOLAR CELL in Terrassa, Barcelona, Spain.

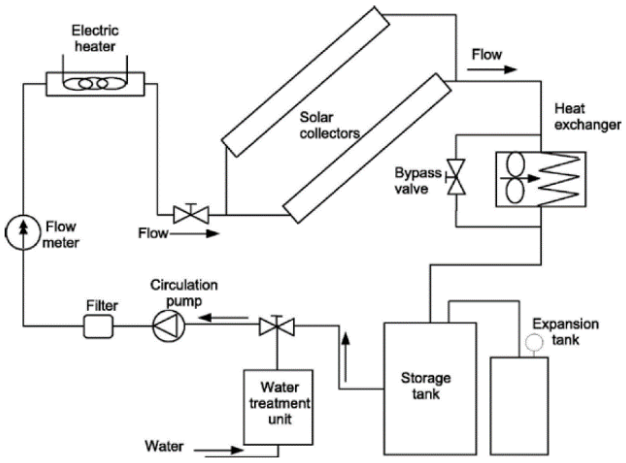

Fig. 9: Test bench used for the thermal characterization of the solar collectors

3.2. Experimental results of the first FPC

The 1st FPC manufactured was optimized using a preliminary numerical method. After running several simulations with that mathematical model, a silica layer of 2 cm was selected. In contrast, the best option for the honeycomb was the 7.5 cm thickness. It is the maximum available thickness in the market and reduces the silica needed to achieve high efficiencies. The other materials' thicknesses were set by manufacturing constraints or were decided to be studied layer on the project.

The glasses used were high transmittance and low emissivity, with a transmittance of 0.92 in the visible spectrum.

A 1st test campaign has been performed to validate the steady-state efficiency obtained by the preliminary numerical model. That model has resulted in overestimating the insulating capacity of the materials used and the optical efficiency of the manufactured FPC, as depicted in Fig 10. Nevertheless, part of the discrepancies observed between experimental and computed data is the manufacturing limitations discussed later.

The implementation of granular silica aerogel in the FPC has improved the first and second-order coefficients while deteriorating the optic efficiency of the FPC compared with previous studies of Kessentini et al. (2014). This behavior, yet expected, due to the implementation on a second glass layer and the silica, was more severe than predicted.

A relevant side-effect was found after the manufacturing of the prototype. Since the silica aerogel is placed between two layers without casing, the silica particles tend to fall to the bottom of the collector when the collector is tilted. This reduces the insulating capacity at the top of the FPC because it leaves some absorber area exposed directly to the second glass layer. This problem will be tackled in future versions of the FPC and discussed in the conclusions.

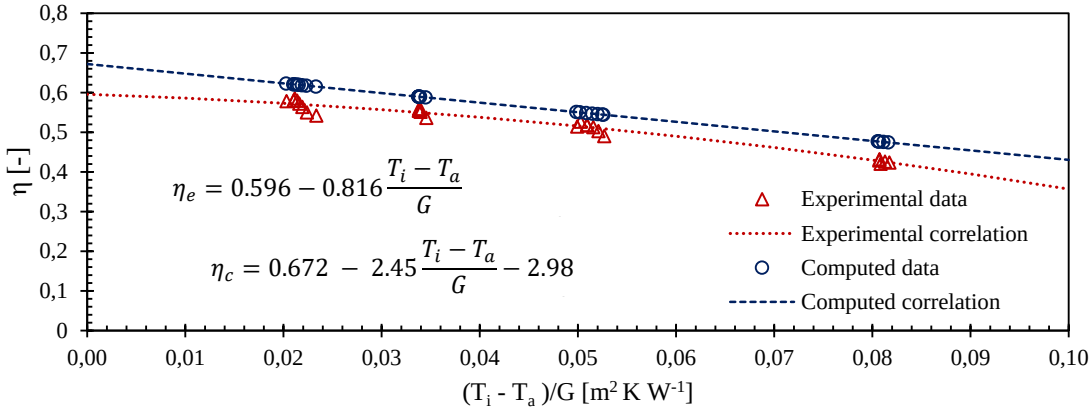

Fig. 10: Preliminary model vs. experimental FPC with transparent insulation materials (honeycomb and silica aerogel).

An important design constrain is the honeycomb temperature limit. Kessentini et al. (2014) implement an overheating protection system placed behind the FPC to avoid this problem. This implementation is intended to be avoided by implementing the silica layer. Once optimizing the FPC, a complete stagnation test will be performed to prove the durability of the TIM layer without a protection system. It is expected that the inner temperatures of the collector were reduced significantly, with good redesign and silica layer stabilization, making this objective potentially achievable.

With all these factors considered, the model was refined following the method described in section 2. of this document and including some parameters to tune the equations to make them closer to the real experimentation constraints. The proposed model introduced a better characterization of the silica layer and considered the honeycomb properties better for the diffuse irradiance (more details in point 2.4).

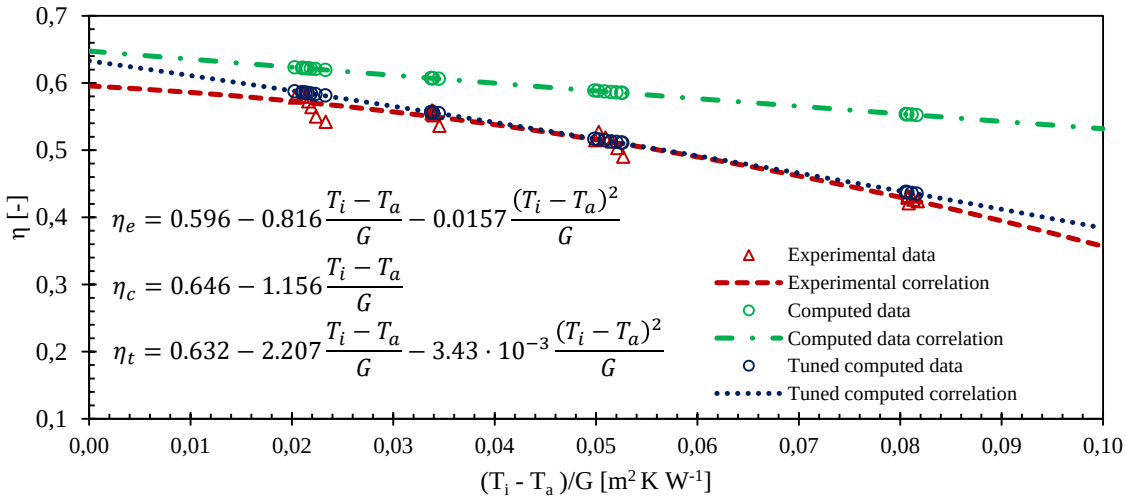

Fig. 11: Proposed model vs. experimental FPC with transparent insulation materials (honeycomb and silica aerogel).

As can be seen in Fig. 11, the proposed model without tuning resulted in, as well, an overestimation of the efficiency of the FPC. However, decent estimation of the experimental data was obtained after adequately adjusting the relevant parameters.

The results show the importance of the parameters that have been tuned to achieve a better approximation of the efficiency of the flat plate collector. Those parameters were the following:

- Silica thickness
- Air-silica compactness ratio

To achieve the results in Fig. 11, the silica thickness was increased by 1cm with respect to the design consideration (2cm), getting a total silica thickness to 3cm. This parameter change is because the absorber plate tends to buckle due to the silica weight and thermal expansion. This was considered in the manufacturing procedure, but the material used in the back of the collector to prevent the deformation has not been enough to keep the absorber in place. As a side-effect, the silica layer has more volume to fill and tends to fall to the bottom of the FPC. To consider the phenomena in the mathematical model, the air-silica compactness ratio is modified to a value of 33%. This ratio can be understood as the volume occupied by air in the silica region. As per manufacturing constraints, there will always be some air in the silica region, and it will never be 0%. The only way to get to the 0% of air would be to use non-granular silica. Which will be discussed in section 5.

Next summer a 2nd test campaign will be performed, taking advantage of the previous experience, and using the refined mathematical model for an optimization analysis with the aim of improving the design and prototyping of the 2nd version of the solar collector.

4. Optimization and parametric study

To optimize the overall performance of the FPC, a parametric study has been conducted by changing three main parameters:

i) The glass transmissivity from 0.92 to 0.96 produces a high optical efficiency increment. This increment can be done by changing the glass used compared to the previous FPC;

ii) Second, the air-silica compactness ratio is set at 15%. Meaningful learning obtained in the 1st FPC design is that a 0% ratio can never be obtained using granulate silica, so it is realistic to recognize a certain degree of air in the silica layer. A 15% seems achievable, improving the casing and preventing some absorber expansion.

iii) Third, several different thicknesses of silica layer to see the impact in the optical efficiency and the first and second order coefficients. The results of the parametric study can be seen in Fig. 12. The results have been compared with the 1st FPC manufactured, a honeycomb collector with a 0.96 transmissivity glass, and the experimental Kessentini et al. (2014) honeycomb collector with 0,92 transmissivity glass.

As can be seen in Fig. 12, the optimal thickness of the silica layer is 1cm. An important conclusion can be obtained. It is better to surpass the 1cm of silica instead of getting less than that since the second order coefficient increases sharply when the silica layer gets closer to 0.5cm. Another remark is that increasing the silica layer above 2cm has more drawbacks than advantages. The optical efficiency gets severely punished and brings the whole efficiency down making useless the improvement in the first and second order coefficients.

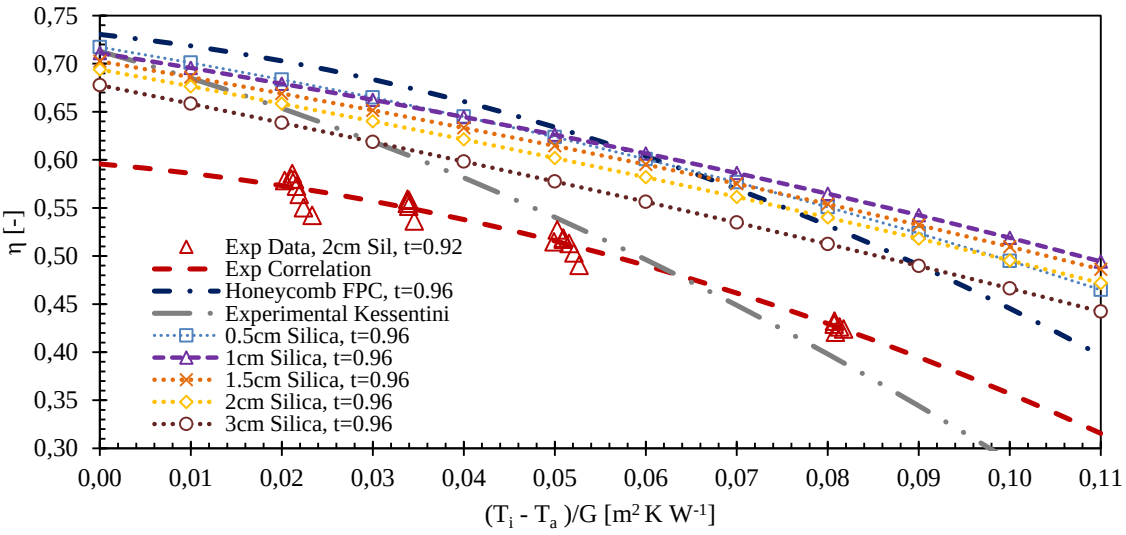

Fig. 12: Optimization of the FPC with transparent insulation materials (honeycomb and silica aerogel) vs. previous versions.

The use of a 0.96 transmissivity glass seems to impact the optical efficiency significantly. It improves the overall efficiency of the FPC for all the thicknesses of the silica layer significantly.

In contrast with the FPC with a honeycomb layer but no silica, the proposed FPC surpasses its efficiency in the high-temperature-difference region as expected with a pretty low impact on the optical efficiency.

Regarding the protection capacity of the silica to the honeycomb layer, as shown in Fig. 13, it is less than optimum since temperatures, for a 1cm silica, get above 100ºC for stagnation conditions at an ambient condition of 20ºC.

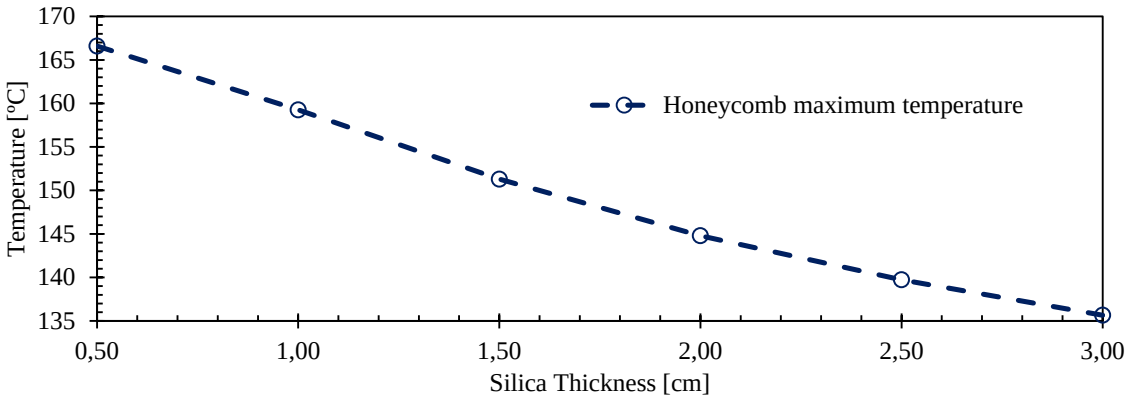

Fig. 13: Honeycomb layer temperature vs. the thickness of the silica layer for stagnation conditions

With a silica layer of 3cm, the FPC efficiency is punished, the temperatures decrease significantly in the honeycomb layer, but still above 130ºC. This issue is something to keep in mind for the next generation prototype because it may force implementing an overheating protection system or a heat evacuation system.

Yet these results are relevant, but uncertainty always needs to be tackled, and the manufacturing limitations can drive those efficiencies down. The best way to assess the effects is to test them experimentally.

5. Future research and direction

After analyzing the results seems that implementing a higher transmissivity glass should be mandatory to improve the performance while paying close attention to the manufacturing details to keep the air-silica compactness ratio as low as possible. Additionally, a silica layer between 1 and 1.5 cm should be targeted to achieve the best possible overall efficiency while it may not be enough to protect the honeycomb layer.

A more detailed overheating analysis should be conducted to assess the honeycomb layer temperatures appropriately and improve the durability of the solar collector.

The use of vacuum techniques to force the compactness of the overall glass-silica-absorber subgroup could be worth the study. Yet, it can make the overall mounting process both complex and expensive.

Finally, monolithic silica dies instead of granulate silica aerogel should improve the overall efficiency for two reasons. The first reason is that the air-silica compactness ratio will be 0%, and the second is because the double glass, placed between the honeycomb and the silica, would not be necessary. This material change should improve both the optical efficiency and the first and second-order coefficients. The only drawback of this design is that the monolithic silica aerogel significantly increases the costs.

6. Conclusions

A crucial factor to consider for the 2nd prototype is to prevent the silica particles from falling by implementing a better manufacturing technique to increase the air-silica compactness ratio, improving insulation. However, the mounting may be more complex.

Moreover, implementing 0,96 transmissivity glass layers should be mandatory to boost performance since

implementing it is notorious.

Finally, in conclusion, the FPC will need a thicker silica aerogel layer or a more compact silica layer to prevent the implementation of an overheating protection system. However, the wider the silica, the lower the maximum temperature achieved in the honeycomb layer. This question will need to be appropriately assessed in the next generation of FPC since increasing too much the silica layer significantly reduces the overall efficiency.

7. Acknowledgments

The authors want to thank the CTTC department's support for permitting the use of the CTTC experimental facility. Special thanks to Jian for his technical support in manufacturing the FPC and his support during the experimental activities.

Sponsored by the SUDOKET – SOE2/P1/E0677 project under the Interreg-Sudoe program

8. References

Giovannetti F., Kirchner M., Rockendorf G., Kehl O., 2011. Cellulose triacetate honeycomb compounds for improved flat-plate collectors: performance and reliability. Proceedings ISES Solar World Congress 2011. doi:10.18086/swc.2011.19.15

Kessentini, H., Castro, J., Oliva, A., 2014. Development of flat plate collector with plastic transparent insulation and low-cost overheating protection system. Applied Energy. 133, 206-223.

Klier, S., Klier, Z., Adel, M., Efron, R., TIGI LTD., 2014. System and method for temperature limiting in a sealed solar energy collector (US Patent Number 8857426B2) Mark M. Friedman. URL: https://patentimages.storage.googleapis.com/48/43/73/b224ddbdaebbc0/US8857426.pdf

Eckert E. R. G., Drake R. M. Jr., 1971. Analysis of Heat and Mass Transfer, McGraw-Hill, New York.

Platzer WJ., 1992. Calculation procedure for collectors with a honeycomb cover of rectangular cross section. Solar Energy. 48(6), 381–93

Appendix: Units and Symbols

Table 1: Symbols for properties

Preferred name	Symbol	Unit
Heat flux	$\dot{q}$	W m^{-2}
Temperature	T	K
Thermal conductivity	k	W m^{-1} K^{-1}
Wall fraction	WF	
Heat transfer coefficient	h	W m^{-2} K^{-1}
Thermal conductivity	k	W m^{-1} K^{-1}
Thickness	e	m
Overall heat loss coef.	U	W m^{-2} K^{-1}
Absorbed solar energy by abs. plate	S	W m^{-2}
Resistance coef.	R	W m^{-2} K^{-1}
Number of tubes	n_t	
Tubes spacing	W	m
Position length	x, y	m
Aperture Area of FPC	A_C	m^2
Perimeter of FPC	P_C	m^2
View factor	F	
Irradiation	$\dot{g}$	W m^{-2}
Radiosity	j	W m^{-2}
Emittance	ε	
Reflectance	ρ	
Efficiency	η	
Solar irradiance on FPC	G	W m^{-2}

Table 2: Suffixes for properties

Suffixes	Symbol
Radiative heat	rad
Convective heat	conv
Conductive heat	cond
Transmitted heat	trans
Visible spectrum	s
Infrared spectrum	t
Cover glass	c1
Honeycomb	TIM
Interior glass	c2
Silica aerogel	sil
Absorber	abs
Vector perpendicular to collector plane and pointing up	ext
Vector perpendicular to collector plane and pointing down	int
Ambient	a
Positional index or inlet	i
Outlet	o
Fin	fin